

Enhancing the Efficiency of Complex Systems Crystal Structure Prediction by Active Learning Guided Machine Learning Potential

Jiaxiang Li,¹ Junwei Feng,² Jie Luo,^{1,3} Bowen Jiang,¹ Xiangyu Zheng,¹ Jian Lv,¹ Keith Butler,⁴ Hanyu Liu,^{1,3,5,*} Congwei Xie,^{2,†} Yu Xie,^{1,6,‡} and Yanming Ma^{1,3,5}

¹Key Laboratory of Material Simulation Methods & Software of Ministry of Education, College of Physics, Jilin University, Changchun 130012, China

²Research Center for Crystal Materials, State Key Laboratory of Functional Materials and Devices for Special Environmental Conditions, Xinjiang Key Laboratory of Functional Crystal Materials, Xinjiang Technical Institute of Physics and Chemistry,

Chinese Academy of Sciences, 40-1 South Beijing Road, Urumqi 830011, China

³State Key Laboratory of Superhard Materials, College of Physics, Jilin University, Changchun 130012, China

⁴Department of Chemistry, University College London, Gordon Street, London, WC1H 0AJ, UK

⁵International Center of Future Science, Jilin University, Changchun 130012, China

⁶Key Laboratory of Physics and Technology for Advanced Batteries of Ministry of Education, College of Physics, Jilin University, Changchun, 130012, China

(Dated: May 14, 2025)

Understanding multicomponent complex material systems is essential for design of advanced materials for a wide range of technological applications. While state-of-the-art crystal structure prediction (CSP) methods effectively identify new structures and assess phase stability, they face fundamental limitations when applied to complex systems. This challenge stems from the combinatorial explosion of atomic configurations and the vast stoichiometric space, both of which contribute to computational demands that rapidly exceed practical feasibility. In this work, we propose a flexible and automated workflow to build a highly generalizable and data-efficient machine learning potential (MLP), effectively unlocking the full potential of CSP algorithms. The workflow is validated on both Mg–Ca–H ternary and Be–P–N–O quaternary systems, demonstrating substantial machine learning acceleration in high-throughput structural optimization and enabling the efficient identification of promising compounds. These results underscore the effectiveness of our approach in exploring complex material systems and accelerating the discovery of new multicomponent materials.

I. INTRODUCTION

Functional materials with unique physical and chemical properties are essential for advancing cutting-edge technologies and driving breakthroughs across various disciplines[1–5]. Compared to simple systems, multicomponent materials with intricate atomic configurations and vast compositional diversity enable fine-tuning of electronic, magnetic, and structural properties, thus offering significantly greater opportunities for discovering a wide range of high-performance functional materials[6, 7]. Examples include high T_c superconductors[8–11], multifunctional alloys[12, 13], high ionic conductivity solid electrolytes[14], and nonlinear optical materials[15–18]. However, the design of multicomponent complex materials remains a major challenge. The combinatorial explosion results in highly complex thermodynamic phase diagrams, while structural diversity[19] and the scarcity of comprehensive data [20] further hinder both experimental and computational exploration, particularly when materials are expected to exhibit both thermodynamic synthesizability and superior functional properties. Given the vast combinatorial complexity of arranging chemical elements from the periodic table into all possible stoichiometries, current knowledge likely captures only a small fraction of the

immense material design landscape[21]. Therefore, advanced techniques are essential for efficiently navigating this space and fully unlocking the potential of complex material systems.

Among theoretical materials design approaches, crystal structure prediction (CSP)[22–32] has emerged as an indispensable tool for predicting stable crystalline configurations prior to experimental synthesis[33–39]. Fundamentally, CSP approaches can be formulated as global (or multi-local) optimization problems on high-dimensional energy surfaces, thereby making accurate free energy calculations essential for reliable predictions. In practice, most conventional CSP implementations employ density functional theory (DFT)[40] as their computational backbone. Despite its reliability, DFT involves solving the electronic structure through an iterative self-consistent field (SCF) procedure, with computational costs scaling cubically with system size ($\sim O(N^3)$ for N electrons). Such unfavorable scaling renders structural searches computationally expensive, thereby restricting most applications to small unit cells with limited compositional complexity. Consequently, the full potential of CSP methods are significantly constrained.

Trained on datasets derived from DFT calculations, machine learning potentials (MLPs) can faithfully reproduce DFT-level potential energy surfaces (PESs) while delivering computational speedups by several orders of magnitude. Research efforts such as GAP-RSS[41], DP-CALYPSO[42], MTP-USPEX[43], and MAGUS[29] demonstrate the feasibility of this paradigm. These approaches typically begin with a concurrent learning sampling scheme to construct a repre-

* hanyuliu@jlu.edu.cn

† cwxie@ms.xjb.ac.cn

‡ xieyu@jlu.edu.cn

sentative DFT dataset along with a corresponding potential model, which is then used to drive CSP for discovering further unknown structures. However, due to the interpolative nature of MLPs, their performance heavily relies on the quality of the dataset. When applied to more complex systems, where the number of relevant local minima increases exponentially[23], assessing whether an MLP can generalize well enough to reliably predict unforeseen configurations is often nontrivial. The risks includes leading CSP to converge to unphysical local minima, thereby compromising the reliability of structure prediction and potentially overlooking meaningful configurations. Recently, an alternative direction has focused on constructing foundation models trained on extensive datasets spanning the whole periodic table[44–51]. Although significant improvements in generalization capability have been observed, the fundamental limitation remains unresolved, especially with data scarcity under extreme pressure conditions, strongly correlated systems, or low-symmetry and defect-rich systems. A robust approach for rapid and exhaustive structural prediction of multicomponent complex systems remains urgently needed.

In this work, we first implemented an MLP, named the attention coupled neural network (ACNN), which demonstrated both high accuracy and computational efficiency in surrogating the PES. Base on ACNN, we developed an automated pipeline specifically tailored to address the challenges of predicting structures for materials with multicomponent variable stoichiometry. At the core of this pipeline is a flexible active learning process that orchestrates the dynamic training of the ACNN and the CSP procedure, ensuring that the ACNN model consistently maintains strong generalization capability throughout. Concurrently, the continuous identification of new structures drives the ongoing refinement of phase diagrams. We validated our algorithm by exploring the high-pressure, defect-rich Mg–Ca–H ternary and Be–P–N–O quaternary systems across expanded compositional and structural spaces. Our approach enabled the optimization of structures with quantities several orders of magnitude greater than those achievable by DFT, significantly broadening the structural search space. Both cases uncovered a wide range of novel, thermodynamically synthesizable materials, including high-temperature superconductors and nonlinear optical materials, highlighting the high data efficiency and low computational cost of our method.

II. METHODOLOGY

A. Machine learning potential

ACNN incorporates various features extensively discussed in previous studies[52–59]. In particular, it explicitly describes intrinsic translational, rotational, and permutational invariance for scalar quantities (energy), and rotational equivariance for tensorial properties (atomic forces and stress tensors). Additionally, the consistently continuous and smooth differentiability should also be satisfied. Following Behler and Parrinello [52], the total potential energy E is expressed

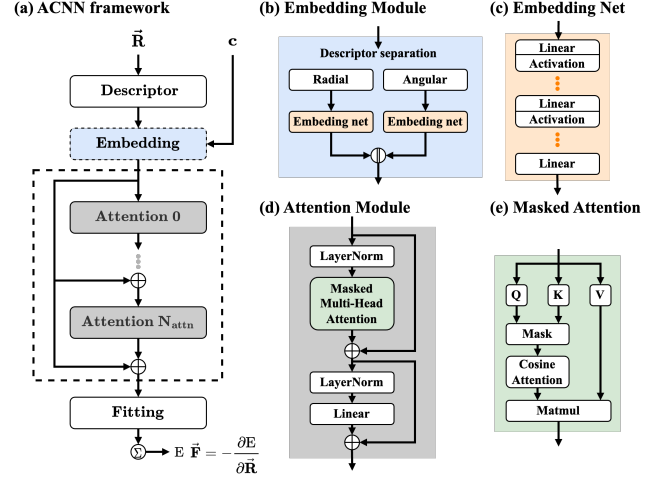


FIG. 1. Schematic illustration of the ACNN architecture and its modular decomposition.

as a sum of atomic contributions E_i .

$$E = \sum_i^N E_i, \quad (1)$$

where N denotes the total number of atoms. The force and virial tensors are directly computed from E via

$$\mathbf{F}_i = -\nabla_i E, \text{ and } \mathbf{W}_i = \sum_{j \neq i} \mathbf{r}_{ij} \otimes \frac{\partial E_i}{\partial \mathbf{r}_{ji}}. \quad (2)$$

The central term E_i is uniquely defined by the local environment \mathbf{R}_i of atom i ,

$$E_i(\mathbf{R}_i) = E(\mathbf{r}_{i1}, \mathbf{r}_{i2}, \dots, \mathbf{r}_{iN}), \quad (3)$$

in which $\mathbf{r}_{ij} = \mathbf{r}_j - \mathbf{r}_i$ denotes the relative position vector from atom i to atom j . ACNN utilizes an analytical descriptor of \mathbf{R}_i , whose form is derived from the atomic cluster expansion (ACE)[58, 60] framework. Specifically, the atomic energy E_i is expanded in terms of v -body correlation functions,

$$\Phi^{(v)}(\mathbf{r}_{ij_1}, \dots, \mathbf{r}_{ij_v}). \quad (4)$$

The energy is obtained through the nonlinear combination effects of the neural network, expressed as

$$E_i(\mathbf{R}_i) = \sum_{v=1}^{V_{\max}} \sum_v \mathbf{c}_v \sum_{j_1, \dots, j_v} \Phi^{(v)}(\mathbf{r}_{ij_1}, \dots, \mathbf{r}_{ij_v}), \quad (5)$$

where \mathbf{c}_v are model parameters associated with the neural network architecture. Typically, the interaction is limited to a predefined cutoff sphere with radius r_c . To smooth the behavior of atoms at the boundary, an envelope function is defined as

$$f_c(r_{ij}) = \begin{cases} \frac{1}{2} \left[1 + \cos\left(\pi \frac{r_{ij}}{r_c}\right) \right] & r_{ij} \leq r_c \\ 0 & r_{ij} > r_c \end{cases}. \quad (6)$$

For a central atom i , the first-order term, which accounts for pairwise interactions, is given by

$$\Phi_n^{(1)} = \sum_{j \neq i} g_n(r_{ij}), \quad (7)$$

where $g_n(r_{ij})$ is a function of the distance, defined as

$$g_n(r_{ij}) = \frac{1}{2} \left[T_n \left(2 \left(\frac{r_{ij}}{r_c} - 1 \right)^2 - 1 \right) + 1 \right] f_c(r_{ij}), \quad (8)$$

with T_n denoting the Chebyshev polynomial of the first kind of order n . The second-order term, which incorporates angular dependencies, is given by

$$\Phi_{nl}^{(2)} = \frac{2l+1}{4\pi} \sum_{j \neq i} \sum_{k \neq i} g_n(r_{ij}) g_n(r_{ik}) P_l(\cos \theta_{ijk}), \quad (9)$$

where $P_l(\cos \theta_{ijk})$ is the Legendre polynomial of order l , and θ_{ijk} is the angle between the vectors r_{ij} and r_{ik} . In general, incorporating higher-order terms improves the completeness of the local environment description and thereby enhances accuracy. However, achieving convergence becomes progressively slower, as evidenced by the tests provided in Drautz [60]. To balance computational efficiency and precision, ACNN explicitly incorporates up to 3-body interactions, while delegating the remaining residual errors to the nonlinear neural network for further correction.

The overall ACNN architecture consists of three main components: an embedding module, an optional stack of attention modules, and a fitting module, as illustrated in FIG. 1. The data flows through these components sequentially. The vectorized geometry of the input structures is first processed by the embedding module, which incorporates elemental information to enrich the feature space. Specifically, the embedding module employs two separate multilayer perceptron networks (FIG. 1(b) and (c)) to independently embed $\Phi^{(1)}$ and $\Phi^{(2)}$ as follows:

$$\Phi = \text{mlp}(\Phi^{(1)}) \parallel \text{mlp}(\Phi^{(2)}), \quad (10)$$

$$\text{where } \text{mlp}(x) = f_L \circ f_{L-1} \circ \dots \circ f_1(x), \quad (11)$$

$$f_l(x) = \tanh(W_l x + b_l). \quad (12)$$

After embedding, the resulting features are either directly fed into the fitting module or passed through one or more attention modules before reaching the fitting stage.

The core of each attention module is a multi-head self-attention layer. From a physical perspective, it can be viewed as a weighted reconstruction of the local atomic neighborhood, where the model learns to infer the relative contributions of neighboring atoms. We adopt the standard formulation[61] for constructing the query, key, and value matrices, given by

$$Q = xW^Q, \quad K = xW^K, \quad V = xW^V \quad (13)$$

$$h = \text{softmax}(S) \cdot V \quad (14)$$

However, we employ a slightly modified score function,

$$S_{ij} = f_c(r_{ij}) \cdot \cos(\mathbf{q}_i, \mathbf{k}_j) / \tau, \quad (15)$$

where τ is a trainable scalar constrained to be greater than 0.01, introduced to automatically scale the attention scores and yield smoother weighting. The fitting module, composed of a multilayer perceptron, simply receives the processed features and pools them to predict atomic energies, as defined by the formulation in Eqs. 11 and 12.

In summary, the ACNN architecture offers a flexible and straightforward framework for implementing and switching between two distinct MLP designs, both of which satisfy the accuracy requirements for CSP. The primary distinction lies in the trade-off between computational cost and accuracy. Introducing attention modules increases model complexity and the number of trainable parameters, thereby enhancing the learning capacity of ACNN. Furthermore, stacking multiple attention modules implicitly introduces an aggregative effect analogous to that of graph neural networks (GNNs) [62], which extends the effective interaction range among atoms. However, this comes at the cost of higher computational overhead and fundamentally limits the applicability of domain decomposition algorithm for efficient parallelization. Therefore, the attention-based ACNN architecture does not meet the computational requirements for large-scale, multicomponent crystal structure prediction tasks of the complex systems considered in this study. Detailed accuracy and computational speed tests are provided in Section S1 of the Supplementary Materials.

B. Training and refining

All parameters c_v in Eq. 5 are trainable through the back-propagation process. Considering that the training set may contain structures with varying numbers of atoms, we define the loss function as follows,

$$L = \frac{1}{N_B} \sum_{i=1}^{N_B} p_e \frac{|E_i - \hat{E}_i|^2}{N_i} + p_f \frac{\|F_i - \hat{F}_i\|^2}{3N_i} + p_w \frac{\|W_i - \hat{W}_i\|^2}{3N_i}. \quad (16)$$

Here, N_B is the minibatch size, and N_i the number of atoms in structure i . Hatted quantities (e.g., \hat{E}_i) represent reference values, whereas unhatted ones correspond to ACNN predictions. p_e , p_f , and p_w are tunable parameters that flexibly adjust the relative contributions of each component in the loss function. We employed the AdamW[63] optimizer, which incorporates L2 regularization to mitigate overfitting by penalizing large parameter values. This may help improve the generalization performance of the ACNN model when trained on a diverse set of structures broadly sampled from the PES.

When applied to CSP, the training set typically needs to be continuously expanded through the active learning process discussed below. Therefore, ACNN supports restarting training or refining the model from any existing checkpoint with a new or updated dataset. In addition, small perturbations can be introduced to the trainable parameters during refinement to reduce the risk of systematic errors in extrapolated predictions. The underlying intention is for the perturbed model to quickly stabilize in well-sampled regions at the start of refinement, while preserving controlled stochasticity in out-of-distribution regions.

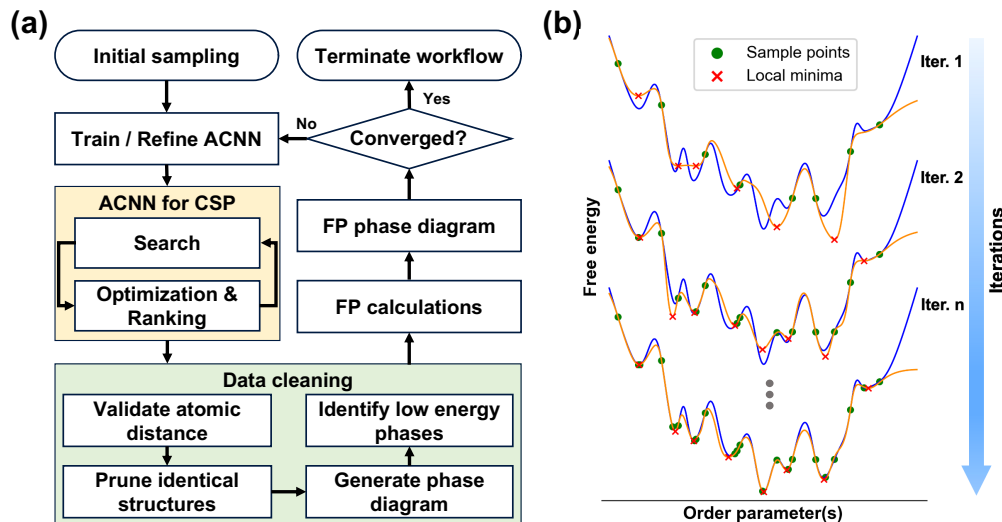


FIG. 2. (a) The scheme of active learning workflow. (b) Illustration of the iterative refinement of ACNN and the structure sampling process in active learning. The conceptual depiction of the DFT energy landscape (blue line) highlights the funnel-like energy valley with multiple local minima. ACNN is iteratively trained on sample points (green dots), leading to a simplified predicted energy landscape (orange line) that retains the key features of the true one.

C. Active learning

As a data-driven paradigm for interatomic potentials, the performance of ACNN highly depends on the quality of the sampling data. Active learning aims to maintain the predictive accuracy and generalization of the ACNN model during the CSP process, while reducing the number of expensive DFT calculations. According to the principle of maximum information gain, two types of structures are particularly necessary to trigger DFT calculations and should be included in the training set. The first type consists of energy-minimum structures. These samples help reduce the discrepancy between ACNN predictions and DFT reference values, guiding the model toward a more accurate surrogate of the PES. The second stems from unphysical local minima, which typically arise from the model’s insufficient representation of certain regions and therefore require further reinforcement.

The flowchart of the active learning pipeline is illustrated in FIG. 2(a), where two types of data acquisition discussed above are naturally integrated. Upon triggering the workflow, a small set of randomly generated structures undergoes DFT self-consistent field (SCF) calculations, which then form the initial training dataset for ACNN. After training, CSP approach is then carried out on the coarse potential until the number of unphysical structures exceeds a threshold B_{max} . This indicating that the model’s generalization capability is no longer sufficient for further reliable exploration. The resulting structures are firstly filtered through fingerprint-based[23, 27] deduplication. Subsequently, a thermodynamic phase diagram is constructed based on ACNN accuracy. Despite being incomplete or suboptimal, early ACNN-derived phase diagrams still offer useful guidance for sampling and model refinement. Here, we adopt a composition-wise selection strategy: we first identify the C_{max} compositions with the lowest

convex hull enthalpies (E_{hull}), and then select the L_{max} lowest-enthalpy structures from each of these compositions. These structures, along with those that fail to converge during optimization, are subsequently subjected to DFT calculations.

The active learning workflow proceeds iteratively, gradually improving the accuracy and generalization of the ACNN model. As its performance advances, more structures are discovered and incorporated into the training set, further reinforcing the model’s capability, as schematically illustrated in FIG. 2(b). Since the sampled dataset also serves as the target for structure prediction, the resulting phase diagram or energy sequence at DFT-level accuracy can be directly constructed from the training data. After sufficient iterations, the phase diagram tends to converge, indicating that the search is approaching exhaustion. Once no additional high value structures are identified, the workflow can be terminated.

Since prediction errors are intrinsic to MLPs, evaluating their influence on the reliability of structure prediction is essential. From the perspective of uncertainty quantification, the error can be decomposed into epistemic and aleatoric components[64]. By systematically sampling underexplored regions of PES, the active learning scheme provides an effective mechanism for reducing epistemic uncertainty, the associated errors can be quantitatively assessed on test sets composed of labeled structures from subsequent iterations. Sources of aleatoric uncertainty mainly contributed by the intrinsic training error of the ACNN approach. Efforts to reduce this uncertainty involve preferentially sampling high-value regions, such as local minima, while avoiding configurations that are far from force equilibrium. Collectively, these errors ultimately manifest as inaccuracies in the predicted energies, forces, and stresses during structure optimization. The energy error, ϵ_E , propagates into the calculation of formation enthalpies, thereby affecting the relative stability of structures

within the phase diagram. The force error, ε_F , determines the equilibrium configurations obtained via structural optimization and influences the extent of structural distortion. The stress error, ε_W , manifests in deviations of lattice parameters and cell geometry, and further impacts the enthalpy through its contribution to the PV term. If these errors are viewed as perturbations to the equilibrium structures, the resulting phase diagrams tend to overestimate the enthalpy of the structures. To achieve more accurate phase boundaries, it is often necessary to perform full DFT structural relaxations for the structures near the convex hull.

D. Computation methods

To assess the effectiveness of the ACNN-based active learning approach in complex material system design, we have conducted systematic tests on two variable composition chemical systems: (i) ternary Mg-Ca-H system, and (ii) quaternary Be-P-N-O system. All known elementary, binary, ternary, and quaternary structures are used as reference structures to evaluate of the thermodynamic stability of newly discovered structures, however, none of them are included a priori in the training set. This ensures a fairer evaluation by more closely reflecting practical application scenarios.

The ACNN hyperparameter configurations for both systems share the following settings: elemental embedding networks with [64, 64] configuration (two layers of 64 neurons), fitting networks with [256, 256] configuration (two layers of 256 neurons), radial basis functions of order $n_{max}^r = 16$, angular basis functions of order $n_{max}^a = 14$, and an angular momentum cutoff of $l_{max} = 4$ for characterizing single-bond interactions. The cutoff distances differ between systems: for the Mg-Ca-H system under high pressure, $r_c^r = 5.0 \text{ \AA}$ and $r_c^a = 4.0 \text{ \AA}$ are used, whereas for the Be-P-N-O system, $r_c^r = 6.5 \text{ \AA}$ and $r_c^a = 6.0 \text{ \AA}$. In each iteration of the active learning workflow, the ACNN is trained for 10^5 backpropagation steps. An exponential decay learning rate schedule is adopted, with the learning rate decaying by a factor of 0.97 every 10^4 steps.

To achieve optimal computational efficiency of ACNN, we employ an in-house implementation of the Broyden-Fletcher-Goldfarb-Shanno (BFGS) algorithm to perform batch structure optimization. The batch mode enables multiple structures to be optimized simultaneously, significantly increasing the degree of parallelism, ensuring efficient utilization of computational resources during the CSP workflow. The convergence criteria were set at an energy threshold of 10^{-6} eV/atom and a force threshold of 10^{-3} eV/\AA for each directional component.

For structure generation, we employ the Crystal Structure Analysis by Particle Swarm Optimization (CALYPSO) code[26, 27] in a purely random sampling mode with only symmetry constraints imposed. This ensures an unbiased evaluation of our approach’s performance by eliminating methodology-specific biases inherent to conventional CSP techniques. Though, the swarm-intelligence-based evolutionary approach has been demonstrated to be highly efficient in practical applications.

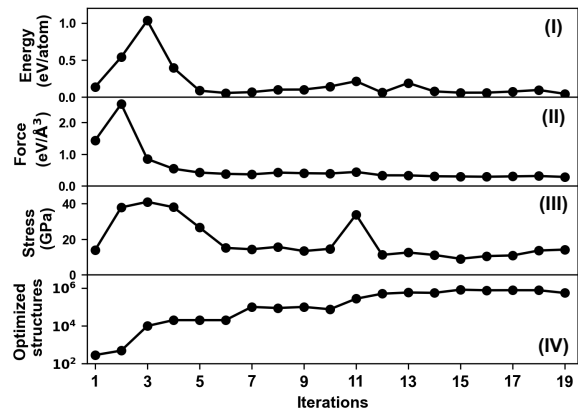


FIG. 3. (I–III) Prediction root mean square errors (RMSEs) for energy, force, and stress at each iteration of the ACNN model. The errors are evaluated using DFT-calculated data from the next generation of sampled structures, tested against the model from the current iteration. (IV) Number of optimized structures obtained in each iteration.

All DFT calculations were performed using the Ab initio material modeling Software (ARES) package [65], within the framework of the generalized gradient approximation level of theory[40], and employing the optimized norm-conserving Vanderbilt pseudopotentials [66, 67] to account for core-electron effects. For the Mg-Ca-H system, the plane-wave and density cutoff energies were set to 70 Ry and 280 Ry, respectively, while for the Be-P-N-O system, they were set to 80 Ry and 320 Ry. Both systems share the same k-point spacings configuration, with $2\pi \times 0.03\text{\AA}^{-1}$ for SCF calculations during structure prediction and $2\pi \times 0.02\text{\AA}^{-1}$ for electronic structure calculations.

III. RESULTS AND DISCUSSION

A. Mg-Ca-H system

Recent breakthroughs in superconductivity research have been achieved through the theoretical prediction of clathrate-type hydride compounds under high pressure, such as CaH_6 [37–39] and LaH_{10} [34–36, 68, 69], which were later confirmed by experimental synthesis. These materials, known as “metal superhydrides”, feature a distinctive structural motif where metal atoms are encapsulated within hydrogen-based clathrate cages. As one of the pioneering examples, CaH_6 exhibits a high superconducting critical temperature (T_c) of 215 K at 172 GPa. Theoretical frameworks suggest that lighter metal atoms exhibit lower frequency vibrational modes that favor superconductivity, along with higher electron-phonon coupling from weaker multicentered hydrogen bonding interactions[70]. These insights have motivated the incorporation of Mg into the Ca–H binary system, forming the ternary Mg–Ca–H system as a potential platform for high-temperature superconductivity.

Previous study by Sukmas *et al.* [71] reported a metal-

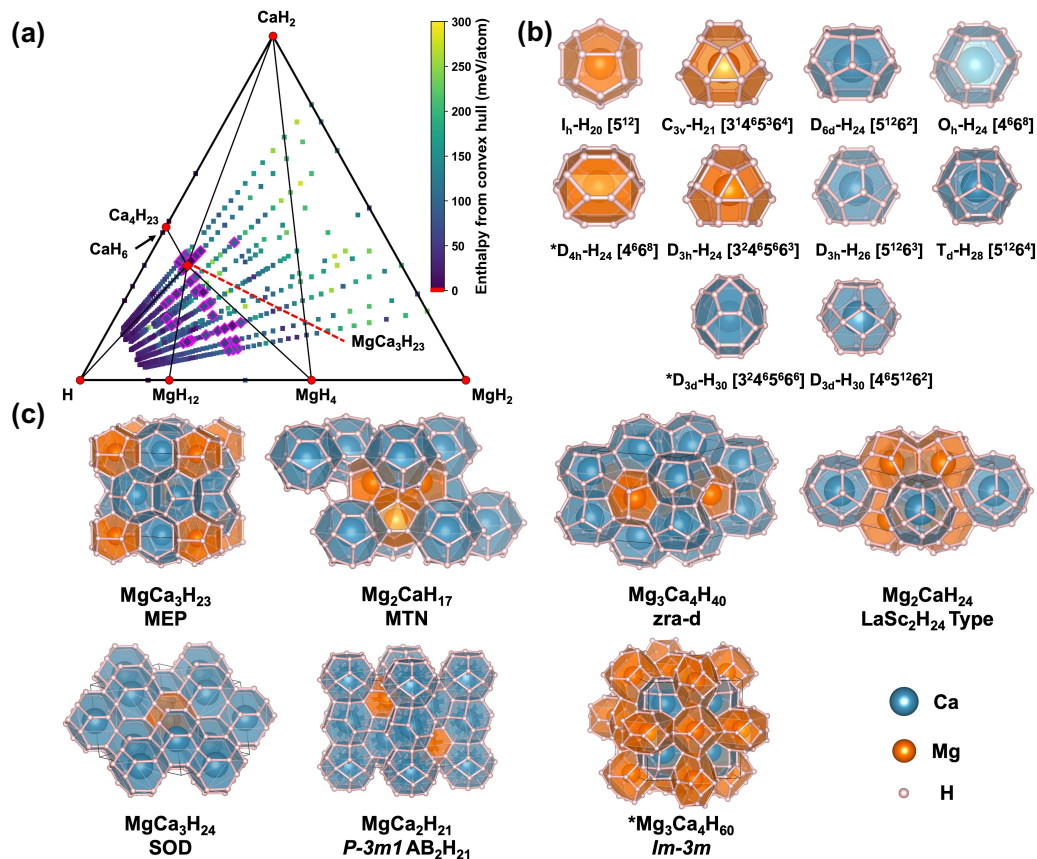


FIG. 4. (a) The phase diagram of MgH₂–CaH₂–H, with cage-like structures indicated by magenta diamonds. (b) Displays the cage units extracted from the corresponding frameworks. The labels follow the format “symmetrical-H_n polygons”. (c) Prototype structures of the predicted cage-like hydrides. Some of them correspond to known frameworks in zeolite databases are labeled accordingly after the formula. Structures not previously reported are marked with asterisk (*).

substituted phase, Mg_{0.5}Ca_{0.5}H₆, derived from the novel *Im* $\bar{3}m$ CaH₆ prototype. This phase was predicted to exhibit near room-temperature superconductivity, with an estimated T_c of 288 K at 200 GPa. More recently, Cai *et al.* [72] successfully synthesized Ca-Mg-based ternary superhydrides using binary intermetallic CaMg₂ and 1:1 Ca-Mg mixture as starting reactants. The resulting compounds exhibited T_c approaching 168 K at 310 GPa in the CaMg₂-based superhydride and 182 K in 1:1 the Ca-Mg superhydride at 324 GPa. These findings indicate the existence of high T_c compound in this system. However, due to the prohibitive computational cost of exploring the vast ternary space, a comprehensive ternary phase diagram remains elusive.

Herein, we conduct a variable stoichiometry structure search at 300 GPa. For the composition space, we restrict the number of Ca and Mg atoms to fewer than 4 each, with the maximum hydrogen-to-metal atomic ratio capped at 16. This resulting in a total of 827 irreducible compositions. Additionally, a constraint of a maximum of 80 atoms per unit cell was imposed, primarily to ensure the inclusion of complex cage-type hydride structures. These settings ensure a sufficiently broad search space, guaranteeing the target structure falls within the search range. Finally, leveraging the high

computational efficiency of the ACNN, a total of 5,964,338 structures were optimized during the CSP stage within approximately 2.7 days on a 192-core AMD EPYC 9654 CPU node, achieving a throughput of 474 structures per core-hour.

Following the active learning protocol, DFT SCF calculations were performed on an initial set of 500 randomly generated structures to initiate the computational workflow. The workflow was iteratively executed for a total of 19 cycles. In each iteration, 300 compositions exhibiting the lowest predicted E_{hull} values ($C_{\text{max}} = 300$) were first selected. From each of these compositions, the 3 lowest energy structures ($L_{\text{max}} = 3$) were then chosen as PES sampling candidates for subsequently DFT calculations. In other words, this regulates the computationally expensive yet necessary DFT calculation to a maximum of 900 optimal structures per iteration. The prediction errors for energy, force, and stress, evaluated by comparing the dataset from the n -th iteration with the ACNN model trained in the $(n - 1)$ -th iteration, are shown in FIG. 3. This validation scheme quantitatively reflects the performance of the ACNN model in predicting potentially unseen local minima structures. The overall decreasing trend in validation error indicates the model’s improving generalization capability with each iteration. By the final iteration,

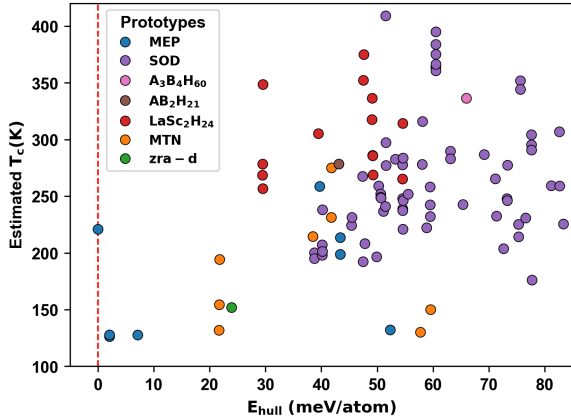


FIG. 5. Superconducting T_c values estimated using the SISSO-based model proposed by Jiang *et al.* [75].

the ACNN achieved a root mean square error (RMSE) of 44 meV/atom for energy, 283 meV/Å for force, and 14 GPa for cell stresses predictions. This continuous improvement is further evidenced by the progressive increase in the number of uninterrupted structure optimization sequences (as shown in FIG 3(IV)).

Finally, 17, 401 structures were automatically sampled for DFT calculations, including 1, 115 structures necessary to correct unphysical descriptions of the ACNN model, and the remaining 16, 286 nearly local minima structures identified as high value candidates. Among these, 8, 994 structures exhibited energy above the convex hull (E_{hull}) below 100 meV/atom. For convex hull refinement, we performed DFT structural relaxation on the 1,000 most stable configurations, with a maximum E_{hull} of approximately 49 meV/atom. As a result, we obtain the phase diagram shown in FIG 4 (a), where a thermodynamically stable $Pm\bar{3}n$ $Mg_2Ca_6H_{46}$ is successfully located. This structure features a hydrogen network adopting the ‘MEP’ zeolite-type topology [73], with Mg and Ca occupying the 2a and 6d Wyckoff sites, respectively. Alternatively, it can also be viewed as a Mg-substituted variant of the recently reported Ca_8H_{46} phase[74], suggesting its a potential high-temperature superconductor. Here, we found $T_c = 137$ K at 300 GPa.

Due to the characteristic features of hydride structures, ideal metal superhydride crystal phases are often accompanied by numerous hydrogen-deficient structures, which typically exhibit comparable formation enthalpies. To efficiently expand the pool of candidate clathrate hydrides, we adopt the screening strategy developed by Jiang *et al.* [75]. This strategy employs an automated topological analysis to identify and classify prototype hydrogen cage motifs. Interestingly, the result accommodates multiple metastable structural prototypes previously reported in zeolite database[76, 77] or other metal hydride systems[78, 79] (see FIG 4 (b)(c)), marked by magenta hollow diamonds in FIG4(a). Nevertheless, we report a new metastable $Im\bar{3}m$ $Mg_3Ca_4H_{60}$ phase with an E_{hull} of 66 meV/atom at 300 GPa. In this structure, Mg and Ca atoms occupy the 6b and 8c Wyckoff sites respectively, forming two

unusual Mg-centered H_{24} cage with D_{4v} point group symmetry and Ca-centered H_{30} cage with D_{3d} symmetry. The H–H bond lengths within these cages measure 0.94, 1.10, 1.11, 1.17 and 1.19 Å at 300 GPa, comparable to those observed in known superconducting hydrogen-rich clathrates, such as CaH_6 (1.24 Å at 150GPa)[37] and LaH_{10} (1.07 and 1.16 Å at 300 GPa)[34, 68].

Building upon the identified candidates structures, we further evaluated their T_c using the SISSO-based prediction model developed by Jiang *et al.* [75]. This model leveraging the projected density of states of hydrogen at the Fermi level ($PDOS_H$) as an electronic descriptor, in combination with geometric features of the structure facilitates rapid T_c estimation. Benchmarking indicates a mean absolute error of approximately 38 K. The estimated T_c values for these metastable hydrides are presented in FIG5, highlighting the presence of numerous potential high-temperature superconductors that may be experimentally accessible. These results underscore the effectiveness of our algorithm in identifying complex superconducting hydrides with promising properties.

B. Be-P-N-O system

In the second test, we apply our method to a more challenging crystal structure prediction (CSP) task by focusing on quaternary compounds. Quaternary system typically present a significantly more complex structural search space due to their greater compositional and configurational degrees of freedom. A particularly promising application lies in the discovery of nonlinear optical (NLO) crystals suitable for deep ultraviolet (DUV) regions. These crystals generate deep ultraviolet coherent light through frequency conversion, enabling essential applications in ultra high resolution lithography, photochemical synthesis, and high precision micromachining. To date, $KBe_2BO_3F_2$ (KBBF)[15, 80] remains the only practical DUV NLO crystal. However, its strong layering habit[81] has significantly hindered its further commercialization. In contrast, phosphates exhibit diverse non-centrosymmetric (NCS) structures, short UV cutoff edges, and favorable single-crystal growth behavior, making them as strong candidates for the discovery of new NLO materials[82–84]. Given these advantages, the Be-P-N-O system is deemed a suitable test case for evaluating our approach.

Following the same procedure used for the above ternary system, we first established the compositional search space. A key distinction, however, is that rigid charge balance rules under ambient pressure can effectively constrain the compositional search space. To ensure both comprehensive and efficient exploration while incorporating experimentally feasible synthesis pathways, we first systematically constructed pseudo-binary phase diagrams based on known binary and ternary compounds, from which all appearing compositions were incorporated into the CSP search space. To further enrich this space, we added all charge neutral compositions with fewer than 32 atoms per unit cell. In total, 373 irreducible compositions were identified and subsequently scaled to multiple formula units, with unit cell sizes constrained to fewer

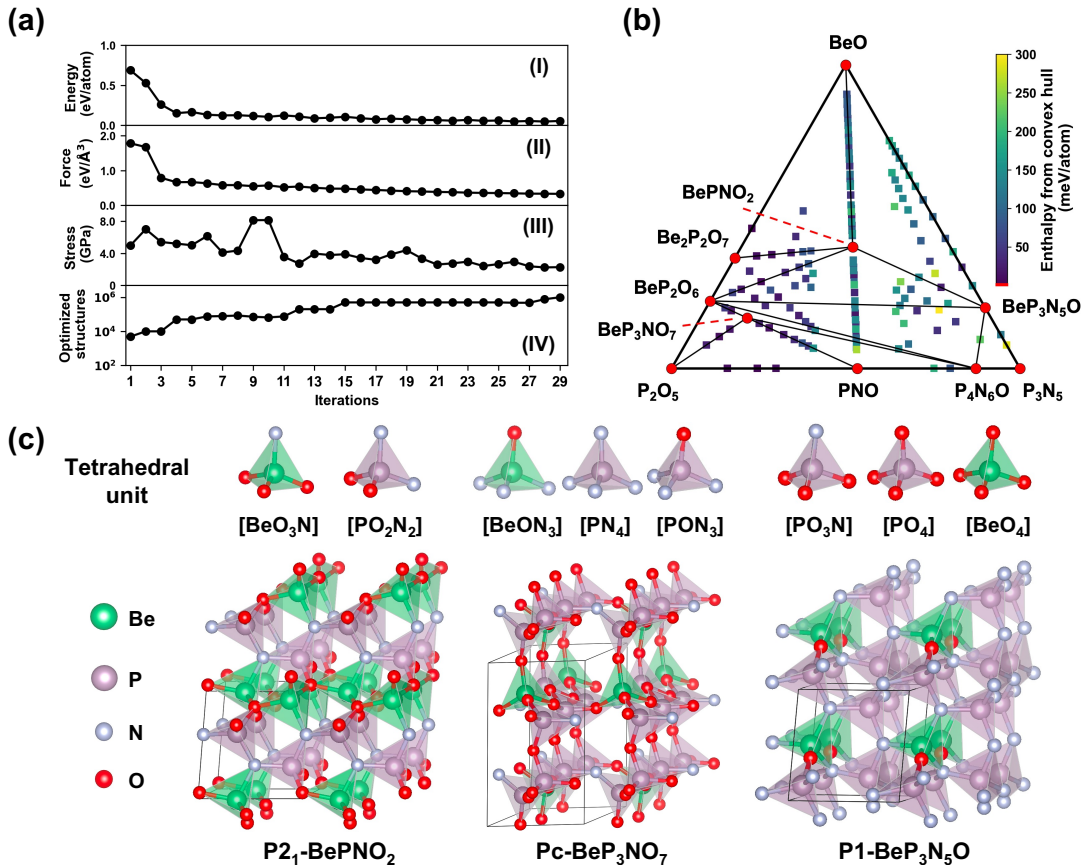


FIG. 6. (a) (I–III) Prediction root mean square errors (RMSEs) for energy, force, and stress at each iteration of the ACNN model. (IV) Number of optimized structures obtained in each iteration. (b) Pseudo-ternary phase diagram of the BeO–P₂O₅–P₃N₅ system, in which three thermodynamically stable phases BePNO₂, BeP₃NO₇, and BeP₃N₅O were located. (c) Three-dimensional (3D) frameworks of stable quaternary Be–P–N–O phases, built from PN_xO_{4–x} and BeN_xO_{4–x} ($x = 1, 2, 3, 4$) tetrahedral units.

than 60 atoms.

A total of 9,381,987 structures were fully relaxed during the CSP stage by ACNN model, executed over 29 active learning iterations to efficiently explore the complex configurational landscape. The entire relaxation process took approximately 1.8 days on a 192-core AMD 9654 CPU, achieving a speed of about 1131 structures per core-hour. Improved relaxation efficiency relative to the previous ternary system primarily attributed to the reduced average number of atoms per structure, as well as the ambient pressure conditions and larger atomic radii (relative to hydrogen) decrease the number of neighboring atoms, collectively lowering the computational workload. For structure sampling, a more flexible strategy was employed. During the initial five iterations, two distinct structures with the lowest energy ($L_{\max} = 2$) were selected from each of the 270 compositions ($C_{\max} = 270$) with the lowest predicted E_{hull} , aiming to facilitate broader exploration of the compositional space. In subsequent iterations, the sampling parameters were adjusted to $L_{\max} = 4$ and $C_{\max} = 95$ to more densely probe novel structures within the compositional region that had been largely validated as near the convex hull and potentially thermodynamical stable.

The corresponding prediction errors during each iterations are presented in FIG6(a). The quaternary system exhibits a more gradual decline in validation error, consistent with the observed trend reported by Wang *et al.* [42] when transitioning from binary to ternary systems. This slower convergence likely arises from the increased structural complexity of higher-order systems, which imposes greater demands on both CSP and the generalization capacity of the MLP. The ACNN model ultimately achieves a RMSE of 62 meV/atom for energy, 325 meV/Å for forces, and 2.2 GPa for cell stresses predictions.

A total of 13,214 structures were selected for SCF calculations, comprising 11,460 local minima and 1,754 unphysical configurations mistakenly predicted as low-enthalpy by ACNN. Among these, top 1,000 structures with the lowest E_{hull} values were subjected to full DFT structural optimization to construct a more accurate convex hull surface. The complete quaternary phase diagram is presented in the Supplementary Information. Three thermodynamically stable phases were identified: $P2_1$ -BePNO₂, Pc -BeP₃NO₇, and $P1$ -BeP₃N₅O. These phases are distributed within the pseudo-ternary compositional space spanned by BeO–P₂O₅–P₃N₅, as

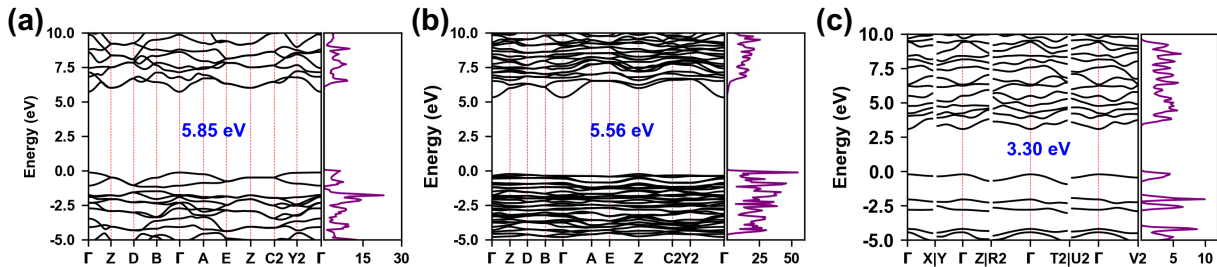


FIG. 7. Calculated band structures, density of states (DOS) of (a) $P2_1$ -BePNO₂, (b) Pc -BeP₃NO₇, and (c) P_1 -BeP₃N₅O.

shown in FIG 6(b). As illustrated in FIG 6(c), the crystal structures of all three phases are composed of P-centered and Be-centered tetrahedra, interconnected through corner sharing to form robust three-dimensional (3D) frameworks with distinctive cavity geometries. This structure structural motif resembles those reported in prior studies[85, 86], where nitrogen atoms partially substitute oxygen within phosphate frameworks, forming PN_xO_{4-x} ($x = 1, 2, 3, 4$) mixed anionic tetrahedra. Such hybrid coordination environments contribute to the structural diversity and potential functionality of these materials.

The electronic band structures of the thermodynamically stable phases are presented in FIG.7, revealing band gaps of 5.85 eV (212 nm), 5.56 (223 nm), and 3.3 (376 nm), as calculated at the PBE level. While it is well-established that PBE tends to underestimate band gaps, the first two phases remain within the DUV spectral range, suggesting their potential for DUV optical applications. Additionally, the resulting structure pool include nearly 3,000 structures with formation enthalpies within $E_{hull} < 100$ meV/atom, commonly associated with potential experimental synthesizability. A more comprehensive analysis of the physical properties of these metastable candidates will provided in a separate forthcoming work.

IV. CONCLUSIONS

In summary, we present ACNN integrated with the CSP technique to establish an efficient and robust active learning workflow aimed at addressing the high computational complexity inherent in predicting complex multicomponent systems. The robust active learning scheme and the effectiveness of the ACNN leverages the ability to explore millions of candidate structures across various stoichiometries and large atomic configurations, enable a more comprehensive investigation of complex systems. We first apply the algorithm to the high pressure Mg-Ca-H system as a test case, where we dis-

cover a stable $Pm\bar{3}n$ MgCa₃H₂₃ phase along with a series of metastable candidates as promising high- T_c superconductors. We further demonstrate the effectiveness of our method on the more complex quaternary Be-P-N-O system. In this case, we identify two potential DUV NLO crystals: $P2_1$ -BePNO₂ and Pc -BeP₃NO₇. Both cases not only corroborate the rich diversity of promising compounds in complex multicomponent systems, but also highlight the capability of our algorithm to efficiently discover functional materials within vast and high-dimensional chemical spaces.

The modular design of the active learning framework offers significant flexibility for application and external integration. This enables dynamic adjustments to the sampling strategy and search space during runtime, as demonstrated in the quaternary Be-P-N-O case above. The ACNN software package is released alongside the first-principles simulation code ARES, forming a technically integrated and robust software ecosystem. By facilitating software-hardware co-design and optimization, this integration fully unleashes the potential of ACNN for materials design and downstream property simulations. Such software design principles provide a computational foundation for automated materials discovery.

ACKNOWLEDGMENTS

This work is supported by the National Key R&D Program of China (Grant No. 2023YFB3003001), the National Natural Science Foundation of China (Grant No. 12374008 and 12022408), the Interdisciplinary Integration and Innovation Project of JLU, and Fundamental Research Funds for the Central Universities and the Program for JLU Science and Technology Innovative Research Team (JLUSTIRT). We also thank the Changchun Computing Center and the Eco-Innovation Center for providing comprehensive computing resources and technical support throughout the completion of this work.

-
- [1] M. A. Green, A. Ho-Baillie, and H. J. Snaith, The emergence of perovskite solar cells, *Nature photonics* **8**, 506 (2014).
 [2] G. Ceder, Y.-M. Chiang, D. Sadoway, M. Aydinol, Y.-I. Jang, and B. Huang, Identification of cathode materials for lithium

- batteries guided by first-principles calculations, *Nature* **392**, 694 (1998).
 [3] C. Liu, H. Chen, S. Wang, Q. Liu, Y.-G. Jiang, D. W. Zhang, M. Liu, and P. Zhou, Two-dimensional materials for next-

- generation computing technologies, *Nature Nanotechnology* **15**, 545 (2020).
- [4] J. K. Nørskov, T. Bligaard, J. Rossmeisl, and C. H. Christensen, Towards the computational design of solid catalysts, *Nature chemistry* **1**, 37 (2009).
- [5] N. P. De Leon, K. M. Itoh, D. Kim, K. K. Mehta, T. E. Northup, H. Paik, B. Palmer, N. Samarth, S. Sangtawesin, and D. W. Steuerman, Materials challenges and opportunities for quantum computing hardware, *Science* **372**, eabb2823 (2021).
- [6] A. Walsh, The quest for new functionality, *Nature chemistry* **7**, 274 (2015).
- [7] H. Lu, J. Tournet, K. Dastafkan, Y. Liu, Y. H. Ng, S. K. Karuturi, C. Zhao, and Z. Yin, Noble-metal-free multicomponent nanointegration for sustainable energy conversion, *Chemical Reviews* **121**, 10271 (2021).
- [8] J. G. Bednorz and K. A. Müller, Possible high T_c superconductivity in the $ba-1-x$ - $cu-x$ system, *Zeitschrift für Physik B Condensed Matter* **64**, 189 (1986).
- [9] Y. Kamihara, T. Watanabe, M. Hirano, and H. Hosono, Iron-based layered superconductor $La_{1-x}Fex$ ($x=0.05-0.12$) with $T_c=26$ K, *Journal of the American Chemical Society* **130**, 3296 (2008).
- [10] H. Sun, M. Huo, X. Hu, J. Li, Z. Liu, Y. Han, L. Tang, Z. Mao, P. Yang, B. Wang, *et al.*, Signatures of superconductivity near 80 K in a nickelate under high pressure, *Nature* **621**, 493 (2023).
- [11] Y. Song, J. Bi, Y. Nakamoto, K. Shimizu, H. Liu, B. Zou, G. Liu, H. Wang, and Y. Ma, Stoichiometric ternary superhydride LaH_8 as a new template for high-temperature superconductivity at 110 K under 80 GPa, *Physical Review Letters* **130**, 266001 (2023).
- [12] G. L. Hart, T. Mueller, C. Toher, and S. Curtarolo, Machine learning for alloys, *Nature Reviews Materials* **6**, 730 (2021).
- [13] M.-H. Tsai and J.-W. Yeh, High-entropy alloys: a critical review, *Materials Research Letters* **2**, 107 (2014).
- [14] Y. Mo, S. P. Ong, and G. Ceder, First principles study of the $Li_{10}GeP_{2}S_{12}$ lithium super ionic conductor material, *Chemistry of Materials* **24**, 15 (2012).
- [15] L. Mei, Y. Wang, C. Chen, and B. Wu, Nonlinear optical materials based on $mbe2b_3f_2$ ($m=na, k$), *Journal of applied physics* **74**, 7014 (1993).
- [16] C. Chen, Y. Wu, A. Jiang, B. Wu, G. You, R. Li, and S. Lin, New nonlinear-optical crystal: LiB_3O_5 , *Journal of the Optical Society of America B* **6**, 616 (1989).
- [17] D. Nikogosyan, Beta barium borate (bbo) a review of its properties and applications, *Applied Physics A* **52**, 359 (1991).
- [18] C. Xie, E. Tikhonov, D. Chu, M. Wu, I. Kruglov, S. Pan, and Z. Yang, A prediction-driven database to enable rapid discovery of nonlinear optical materials, *Science China Materials* **66**, 4473 (2023).
- [19] A. R. Oganov and M. Valle, How to quantify energy landscapes of solids, *The Journal of chemical physics* **130** (2009).
- [20] P. Villars and S. Iwata, Pauling file verifies/reveals 12 principles in materials science supporting four cornerstones given by nature, *Chemistry of metals and alloys*, 81 (2013).
- [21] K. T. Butler, J. M. Frost, J. M. Skelton, K. L. Svane, and A. Walsh, Computational materials design of crystalline solids, *Chemical Society Reviews* **45**, 6138 (2016).
- [22] C. J. Pickard and R. Needs, High-pressure phases of silane, *Physical review letters* **97**, 045504 (2006).
- [23] C. J. Pickard and R. J. Needs, Ab initio random structure searching, *Journal of Physics: Condensed Matter* **23**, 053201 (2011).
- [24] A. R. Oganov and C. W. Glass, Crystal structure prediction using ab initio evolutionary techniques: Principles and applications, *The Journal of chemical physics* **124** (2006).
- [25] A. R. Oganov, C. J. Pickard, Q. Zhu, and R. J. Needs, Structure prediction drives materials discovery, *Nature Reviews Materials* **4**, 331 (2019).
- [26] Y. Wang, J. Lv, L. Zhu, and Y. Ma, Crystal structure prediction via particle-swarm optimization, *Physical Review B—Condensed Matter and Materials Physics* **82**, 094116 (2010).
- [27] Y. Wang, J. Lv, L. Zhu, and Y. Ma, Calypso: A method for crystal structure prediction, *Computer Physics Communications* **183**, 2063 (2012).
- [28] X. Shi, C. He, C. J. Pickard, C. Tang, and J. Zhong, Stochastic generation of complex crystal structures combining group and graph theory with application to carbon, *Phys. Rev. B* **97**, 014104 (2018).
- [29] J. Wang, H. Gao, Y. Han, C. Ding, S. Pan, Y. Wang, Q. Jia, H.-T. Wang, D. Xing, and J. Sun, Magus: machine learning and graph theory assisted universal structure searcher, *National Science Review* **10**, nwad128 (2023).
- [30] Q. Zhu, B. Kang, and K. Parrish, Symmetry relation database and its application to ferroelectric materials discovery, *MRS Communications* **12**, 686 (2022).
- [31] S. Fredericks, K. Parrish, D. Sayre, and Q. Zhu, Pyxtal: A python library for crystal structure generation and symmetry analysis, *Computer Physics Communications* **261**, 107810 (2021).
- [32] X. Shi, C. He, C. J. Pickard, C. Tang, and J. Zhong, Stochastic generation of complex crystal structures combining group and graph theory with application to carbon, *Physical Review B* **97**, 014104 (2018).
- [33] Y. Ma, M. Eremets, A. R. Oganov, Y. Xie, I. Trojan, S. Medvedev, A. O. Lyakhov, M. Valle, and V. Prakapenka, Transparent dense sodium, *Nature* **458**, 182 (2009).
- [34] H. Liu, I. I. Naumov, R. Hoffmann, N. Ashcroft, and R. J. Hemley, Potential high- T_c superconducting lanthanum and yttrium hydrides at high pressure, *Proceedings of the National Academy of Sciences* **114**, 6990 (2017).
- [35] A. Drozdov, P. Kong, V. Minkov, S. Besedin, M. Kuzovnikov, S. Mozaffari, L. Balicas, F. F. Balakirev, D. Graf, V. Prakapenka, *et al.*, Superconductivity at 250 K in lanthanum hydride under high pressures, *Nature* **569**, 528 (2019).
- [36] M. Somayazulu, M. Ahart, A. K. Mishra, Z. M. Geballe, M. Baldini, Y. Meng, V. V. Struzhkin, and R. J. Hemley, Evidence for superconductivity above 260 K in lanthanum superhydride at megabar pressures, *Physical review letters* **122**, 027001 (2019).
- [37] H. Wang, J. S. Tse, K. Tanaka, T. Iitaka, and Y. Ma, Superconductive sodalite-like clathrate calcium hydride at high pressures, *Proceedings of the National Academy of Sciences* **109**, 6463 (2012).
- [38] L. Ma, K. Wang, Y. Xie, X. Yang, Y. Wang, M. Zhou, H. Liu, X. Yu, Y. Zhao, H. Wang, *et al.*, High-temperature superconducting phase in clathrate calcium hydride CaH_6 up to 215 K at a pressure of 172 GPa, *Physical Review Letters* **128**, 167001 (2022).
- [39] Z. Li, X. He, C. Zhang, X. Wang, S. Zhang, Y. Jia, S. Feng, K. Lu, J. Zhao, J. Zhang, *et al.*, Superconductivity above 200 K discovered in superhydrides of calcium, *Nature communications* **13**, 2863 (2022).
- [40] J. P. Perdew, K. Burke, and M. Ernzerhof, Generalized gradient approximation made simple, *Physical review letters* **77**, 3865 (1996).
- [41] V. L. Deringer, C. J. Pickard, and G. Csányi, Data-driven learning of total and local energies in elemental boron, *Physical re-*

- view letters **120**, 156001 (2018).
- [42] Z. Wang, X. Wang, X. Luo, P. Gao, Y. Sun, J. Lv, H. Wang, Y. Wang, and Y. Ma, Concurrent learning scheme for crystal structure prediction, *Physical Review B* **109**, 094117 (2024).
- [43] E. V. Podryabinkin, E. V. Tikhonov, A. V. Shapeev, and A. R. Oganov, Accelerating crystal structure prediction by machine-learning interatomic potentials with active learning, *Physical Review B* **99**, 064114 (2019).
- [44] A. Merchant, S. Batzner, S. S. Schoenholz, M. Aykol, G. Cheon, and E. D. Cubuk, Scaling deep learning for materials discovery, *Nature* **624**, 80 (2023).
- [45] I. Batatia, P. Benner, Y. Chiang, A. M. Elena, D. P. Kovács, J. Riebesell, X. R. Advincula, M. Asta, W. J. Baldwin, N. Bernstein, *et al.*, A foundation model for atomistic materials chemistry, arXiv preprint arXiv:2401.00096 (2023).
- [46] H. Yang, C. Hu, Y. Zhou, X. Liu, Y. Shi, J. Li, G. Li, Z. Chen, S. Chen, C. Zeni, *et al.*, Mattersim: A deep learning atomistic model across elements, temperatures and pressures, arXiv preprint arXiv:2405.04967 (2024).
- [47] F. Xie, T. Lu, S. Meng, and M. Liu, Gptff: A high-accuracy out-of-the-box universal ai force field for arbitrary inorganic materials, *Science Bulletin* **69**, 3525 (2024).
- [48] C. Chen and S. P. Ong, A universal graph deep learning interatomic potential for the periodic table, *Nature Computational Science* **2**, 718 (2022).
- [49] B. Deng, P. Zhong, K. Jun, J. Riebesell, K. Han, C. J. Bartel, and G. Ceder, Chgnet as a pretrained universal neural network potential for charge-informed atomistic modelling, *Nature Machine Intelligence* **5**, 1031 (2023).
- [50] D. Zhang, X. Liu, X. Zhang, C. Zhang, C. Cai, H. Bi, Y. Du, X. Qin, A. Peng, J. Huang, *et al.*, Dpa-2: a large atomic model as a multi-task learner, *npj Computational Materials* **10**, 293 (2024).
- [51] X. Wang, C. Zhang, Z. Wang, H. Liu, J. Lv, H. Wang, Y. Ma, *et al.*, Discovery of high-temperature superconducting ternary hydrides via deep learning, arXiv preprint arXiv:2502.16558 (2025).
- [52] J. Behler and M. Parrinello, Generalized neural-network representation of high-dimensional potential-energy surfaces, *Physical review letters* **98**, 146401 (2007).
- [53] J. Behler, Atom-centered symmetry functions for constructing high-dimensional neural network potentials, *The Journal of chemical physics* **134** (2011).
- [54] A. P. Bartók, M. C. Payne, R. Kondor, and G. Csányi, Gaussian approximation potentials: The accuracy of quantum mechanics, without the electrons, *Physical review letters* **104**, 136403 (2010).
- [55] A. P. Bartók, R. Kondor, and G. Csányi, On representing chemical environments, *Physical Review B—Condensed Matter and Materials Physics* **87**, 184115 (2013).
- [56] A. V. Shapeev, Moment tensor potentials: A class of systematically improvable interatomic potentials, *Multiscale Modeling & Simulation* **14**, 1153 (2016).
- [57] L. Zhang, J. Han, H. Wang, W. Saidi, R. Car, *et al.*, End-to-end symmetry preserving inter-atomic potential energy model for finite and extended systems, *Advances in neural information processing systems* **31** (2018).
- [58] Z. Fan, Y. Wang, P. Ying, K. Song, J. Wang, Y. Wang, Z. Zeng, K. Xu, E. Lindgren, J. M. Rahm, *et al.*, Gpumd: A package for constructing accurate machine-learned potentials and performing highly efficient atomistic simulations, *The Journal of Chemical Physics* **157** (2022).
- [59] S. Batzner, A. Musaelian, L. Sun, M. Geiger, J. P. Mailoa, M. Kornbluth, N. Molinari, T. E. Smidt, and B. Kozinsky, E(3)-equivariant graph neural networks for data-efficient and accurate interatomic potentials, *Nature communications* **13**, 2453 (2022).
- [60] R. Drautz, Atomic cluster expansion for accurate and transferable interatomic potentials, *Physical Review B* **99**, 014104 (2019).
- [61] A. Vaswani, Attention is all you need, *Advances in Neural Information Processing Systems* (2017).
- [62] J. Gilmer, S. S. Schoenholz, P. F. Riley, O. Vinyals, and G. E. Dahl, Neural message passing for quantum chemistry, in *International conference on machine learning* (PMLR, 2017) pp. 1263–1272.
- [63] I. Loshchilov and F. Hutter, Decoupled weight decay regularization, arXiv preprint arXiv:1711.05101 (2017).
- [64] S. Röcken and J. Zavadlav, Accurate machine learning force fields via experimental and simulation data fusion, *npj Computational Materials* **10**, 69 (2024).
- [65] Q. Xu, S. Wang, L. Xue, X. Shao, P. Gao, J. Lv, Y. Wang, and Y. Ma, Ab initio electronic structure calculations using a real-space chebyshev-filtered subspace iteration method, *Journal of Physics: Condensed Matter* **31**, 455901 (2019).
- [66] D. Hamann, Optimized norm-conserving vanderbilt pseudopotentials, *Physical Review B—Condensed Matter and Materials Physics* **88**, 085117 (2013).
- [67] M. J. Van Setten, M. Giantomassi, E. Bousquet, M. J. Verstraete, D. R. Hamann, X. Gonze, and G.-M. Rignanese, The pseudodojo: Training and grading a 85 element optimized norm-conserving pseudopotential table, *Computer Physics Communications* **226**, 39 (2018).
- [68] F. Peng, Y. Sun, C. J. Pickard, R. J. Needs, Q. Wu, and Y. Ma, Hydrogen clathrate structures in rare earth hydrides at high pressures: possible route to room-temperature superconductivity, *Physical review letters* **119**, 107001 (2017).
- [69] F. Hong, L. Yang, P. Shan, P. Yang, Z. Liu, J. Sun, Y. Yin, X. Yu, J. Cheng, and Z. Zhao, Superconductivity of lanthanum superhydride investigated using the standard four-probe configuration under high pressures, *Chinese physics letters* **37**, 107401 (2020).
- [70] E. Snider, N. Dasenbrock-Gammon, R. McBride, X. Wang, N. Meyers, K. V. Lawler, E. Zurek, A. Salamat, and R. P. Dias, Synthesis of yttrium superhydride superconductor with a transition temperature up to 262 k by catalytic hydrogenation at high pressures, *Physical review letters* **126**, 117003 (2021).
- [71] W. Sukmas, P. Tsuppayakorn-ae, U. Pinsook, and T. Bovornratanaraks, Near-room-temperature superconductivity of mg/ca substituted metal hexahydride under pressure, *Journal of Alloys and Compounds* **849**, 156434 (2020).
- [72] W. Cai, V. S. Minkov, Y. Sun, P. Kong, K. Sawchuk, B. Maiorov, F. F. Balakirev, S. Chariton, V. B. Prakapenka, Y. Ma, *et al.*, Superconductivity above 180 k in ca-mg ternary superhydrides at megabar pressures, arXiv preprint arXiv:2312.06090 (2023).
- [73] C. Baerlocher and L. B. McCusker, [Database of zeolite structures](#) (2017), accessed: March 25, 2025.
- [74] D. An, D. Duan, Z. Zhang, Q. Jiang, T. Ma, Z. Huo, H. Song, and T. Cui, Type-i clathrate calcium hydride and its hydrogen-vacancy structures at high pressure, *Physical Review B* **110**, 054505 (2024).
- [75] B. Jiang, X. Luo, Y. Sun, X. Zhong, J. Lv, Y. Xie, Y. Ma, and H. Liu, Data-driven search for high-temperature superconductors in ternary hydrides under pressure, *Physical Review B* **111**, 054505 (2025).
- [76] C. Baerlocher and L. B. McCusker, Database of zeolite structures, <http://www.iza-structure.org/databases/>

- (2017).
- [77] Reticular Chemistry Structure Resource, Reticular chemistry structure resource, <http://rcsr.anu.edu.au/>.
- [78] Y. Sun, J. Lv, Y. Xie, H. Liu, and Y. Ma, Route to a superconducting phase above room temperature in electron-doped hydride compounds under high pressure, *Physical review letters* **123**, 097001 (2019).
- [79] X.-L. He, W. Zhao, Y. Xie, A. Hermann, R. J. Hemley, H. Liu, and Y. Ma, Predicted hot superconductivity in *lasc2h24* under pressure, *Proceedings of the National Academy of Sciences* **121**, e2401840121 (2024).
- [80] C. Chen, G. Wang, X. Wang, and Z. Xu, Deep-uv nonlinear optical crystal *kbe2bo3f2*—discovery, growth, optical properties and applications, *Applied Physics B* **97**, 9 (2009).
- [81] G. Peng, N. Ye, Z. Lin, L. Kang, S. Pan, M. Zhang, C. Lin, X. Long, M. Luo, Y. Chen, *et al.*, *Nh4be2bo3f2* and γ -*be2bo3f*: Overcoming the layering habit in *kbe2bo3f2* for the next-generation deep-ultraviolet nonlinear optical materials, *Ange wandte Chemie* **130**, 9106 (2018).
- [82] S. Zhao, P. Gong, S. Luo, L. Bai, Z. Lin, C. Ji, T. Chen, M. Hong, and J. Luo, Deep-ultraviolet transparent phosphates *rbba2(po3)5* and *rb2ba3(p2o7)2* show nonlinear optical activity from condensation of [po4] 3–units, *Journal of the American Chemical Society* **136**, 8560 (2014).
- [83] H. Yu, J. Young, H. Wu, W. Zhang, J. M. Rondinelli, and P. S. Halasyamani, *M4mg4(p2o7)3* ($m = k, rb$): structural engineering of pyrophosphates for nonlinear optical applications, *Chemistry of Materials* **29**, 1845 (2017).
- [84] L. Li, Y. Wang, B.-H. Lei, S. Han, Z. Yang, K. R. Poeppelmeier, and S. Pan, A new deep-ultraviolet transparent orthophosphate *lics2po4* with large second harmonic generation response, *Journal of the American Chemical Society* **138**, 9101 (2016).
- [85] W. Jin, C. Xie, X. Hou, M. Cheng, E. Tikhonov, M. Wu, S. Pan, and Z. Yang, From monofluorophosphates *a2po3f* to difluorophosphates *apo2f2* ($a = \text{alkali metal}$): Design of a potential deep-ultraviolet nonlinear optical materials system with a shortened phase-matching wavelength, *Chemistry of Materials* **35**, 5281 (2023).
- [86] C. Xie, A. Tudi, and A. R. Oganov, *Pno*: a promising deep-uv nonlinear optical material with the largest second harmonic generation effect, *Chemical Communications* **58**, 12491 (2022).